Chinese Chemical Letters 37 (2026) 111782

Contents lists available at ScienceDirect

Chinese Chemical Letters

journal homepage: www.elsevier.com/locate/cclet

A predictable supramolecular strategy overcomes the aggregation-caused quenching (ACQ) problem in sensitive bioimaging of plant signaling species

Juan Liu[1], Tian Wang[1], Jinghan Yang*, Peiyi Wang*

State Key Laboratory of Green Pesticide, Key Laboratory of Green Pesticide and Agricultural Bioengineering, Ministry of Education, Center for Research and Development of Fine Chemicals of Guizhou University, Guiyang 550025, China

ARTICLE INFO

Article history:
Received 2 April 2025
Revised 16 August 2025
Accepted 1 September 2025
Available online 2 September 2025

Keywords:
Aggregation-caused quenching (ACQ)
Supramolecular technique
Host-guest
Fluorescence probe
Bioimaging

ABSTRACT

Conventional aromatic fluorophores in fluorescent probes can easily initiate molecular aggregation *via* π–π stacking, which drastically quenches fluorescence and hinders cellular permeability. To address this challenge, we developed an ingenious host-guest recognition strategy that converted detrimental π-π stacking into a relaxed molecular aggregation state, enabling the creation of a rhodamine-based supramolecular fluorescent probe called RAO@2CB[8]. This ternary conjugate, assembled by encapsulating adamantyl-modified rhodamine (RAO) with two cucurbit[8]uril (CB[8]), showcased enhanced fluorescence properties for the precise detection of salicylic acid (SA). Intriguingly, in intricate biological systems, RAO@2CB[8] demonstrated exceptional cell permeability, facilitating susceptible detection and imaging of SA in HEK-293 cells, radish roots, and salt-stressed white pea seedlings. This facile supramolecular strategy not only mitigates aggregation-induced quenching, but also provides profound insights for the precise modulation of molecular aggregation behavior.

© 2026 Published by Elsevier B.V. on behalf of Chinese Chemical Society and Institute of Materia Medica, Chinese Academy of Medical Sciences.

Bioactive species, including biogenic acids/amines within living organisms, are pivotal activators regulating biochemical and physiological processes throughout the cell cycle [1–4]. Real-time monitoring of their distributions is crucial for unravelling biological functions and advancing clinical diagnostics. Fortunately, the advent of fluorescence imaging technologies has revolutionized the ability to precisely visualize diverse bioactive species, inspiring scientists to develop novel strategies for life regulation and clinical treatment [5–7]. In cell imaging for bioanalysis, designed fluorescent dyes with exceptional cell permeability, specificity, and sensitivity play an indispensable role. Currently, various fluorochromic scaffolds, including Xanthene, 4,4-difluoroboradiazaindacene (BODIPY) and cyanine, are employed to create fluorescent organic probes [8,9]. These probes have demonstrated remarkable applications in signal sensing and bioimaging. However, conventional aromatic fluorophores are plagued by challenges such as π-π stacking [10,11], background interference [12], and poor water-solubility [13], which collectively diminish their fluorescence efficacy. Among these challenges, the aggregation effect induced by π-π stacking is particularly detrimental, significantly reducing signal sensitivity—a phenomenon known as aggregation-caused quenching (ACQ) [14,15]. This reduction in fluorescence efficacy critically undermines the accuracy of sensors for bioimaging in practical applications, presenting a formidable obstacle to be addressed.

The quest to resolve the ACQ problem has garnered significant attention [16,17]. Scientists are pioneering several strategies to address this challenge, which include: (1) Engineering water-soluble fluorescent probes: Enhancing solubility and dispersibility is crucial to diminish aggregation tendencies [18,19]. (2) Chemical modification with bulky groups: Introducing bulky groups creates a flexible spatial effect, thereby preventing probe aggregation [20,21]. (3) Utilizing organic/inorganic nanocarriers: Loading fluorophores into nanocarriers—such as mesoporous silica and metal frameworks—alleviates π-π stacking by spatially isolating the fluorophores [22,23]. For instance, Ma *et al.* devised a multistep synthesis to construct a water-soluble near-infrared fluorescence probe equipped with large π-conjugated double oxonium ions. This design harnesses ionic repulsion to reduce π-π stacking between fluorophores [24]. In another approach, Seokwoo *et al.* utilized hexadecylamine to modify graphene quantum dots. Consequently, this modification resulted in surface-functionalized graphene quantum dots that effectively circumvent the ACQ ef-

* Corresponding authors.
E-mail addresses: jhyang333@163.com (J. Yang), pywang@gzu.edu.cn (P. Wang).
[1] These authors contributed equally to this work.

https://doi.org/10.1016/j.cclet.2025.111782
1001-8417/© 2026 Published by Elsevier B.V. on behalf of Chinese Chemical Society and Institute of Materia Medica, Chinese Academy of Medical Sciences.

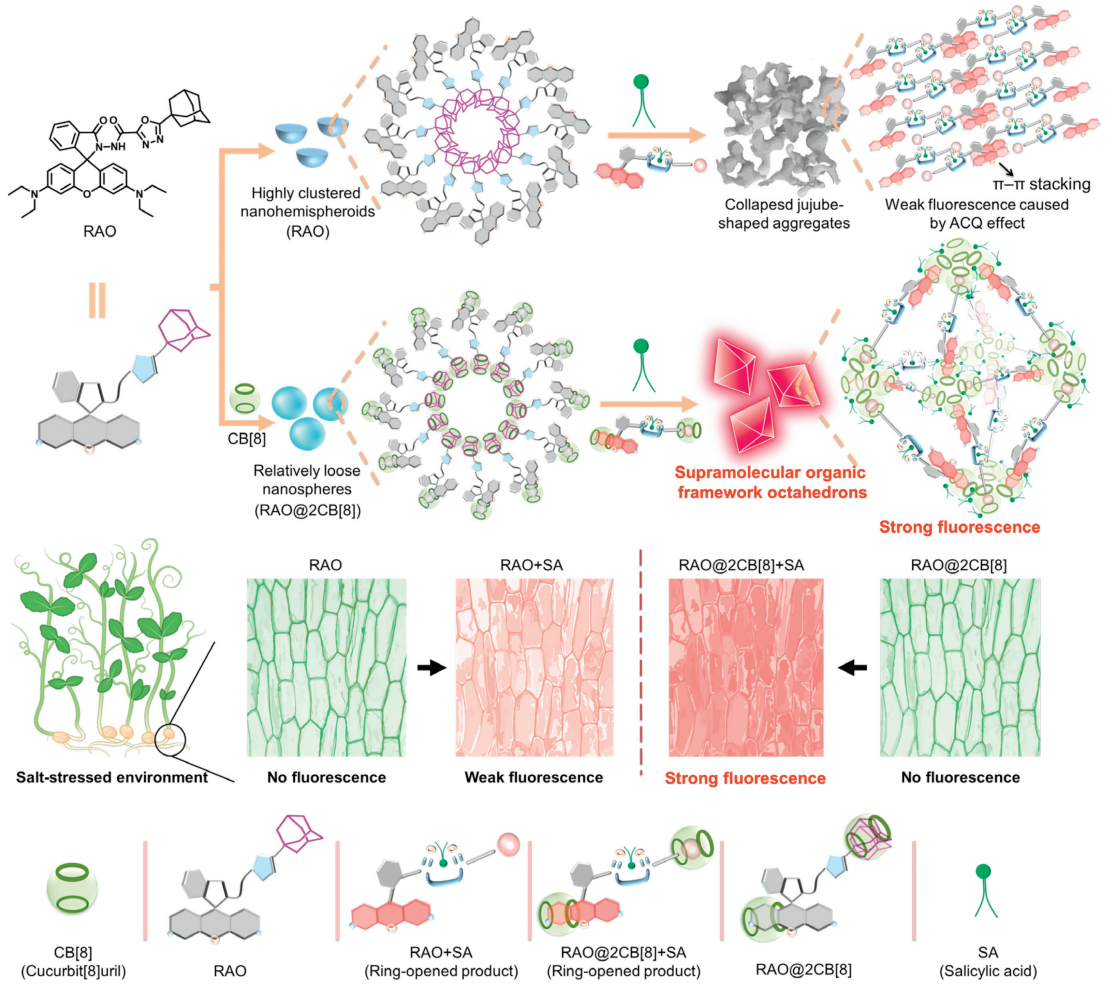
fect [25]. Similarly, Xia and colleagues employed MOFs as carriers to encapsulate fluorescent dyes. This operation mitigated fluorescence quenching caused by dye molecule aggregation, thus facilitating highly sensitive Fe^{3+} detection [26]. With these positive scientific results, considerable progress is made in improving the fluorescence sensitivity of probes. Regrettably, several intractable challenges remain unresolved in practical application. For example, the design considerations and synthetic procedures involved in grafting large groups onto fluorescent probes are both complex and costly [27]. Furthermore, the encapsulation strategy employing porous materials may affect the permeability of the probe [28,29]. Another significant issue is the difficulty in predicting variability in luminescence characteristics attributable to the coupling of encapsulated fluorescent dyes within the carrier material [30–34]. Given these considerations, it is imperative to develop a facile and predictable strategy to avert the π-π stacking effect, perhaps programming to regulate the aggregation behavior of probes at the molecular level.

Recently, supramolecular strategies have presented a promising opportunity to address the aforementioned challenges [35–39]. Supramolecular engineering can regulate the arrangement of molecules into new building blocks, which demonstrate improvements in spatial effects, physicochemical properties [40], biocompatibility [41], and dispersive performance compared to the individual molecules [42,43], unveiling the potence for solving the ACQ problem. Among the non-covalent interactions, the host-guest recognition force stands out due to the host's ability to precisely manipulate guest molecules [44–47]. Macrocyclic hosts, provide guest molecules with appropriate cavities, resulting in proper steric effects that effectively prevent π-π stacking at the molecular level [48–50]. These exciting advantages offer valuable insights for achieving precise detection of bioactive species. Cucurbit[8]uril (CB[8]) owns a pumpkin-shaped cavity, offering outstanding performance in accurately identifying guest molecules, including adamantane, fluorescent dyes, and cationic molecules [51–53]. Importantly, CB[8]'s rigid cavity restricts intramolecular rotation, preventing non-radiative decay and inhibiting the ACQ problem caused by the tight stacking of fluorophores [54,55]. Certainly, this predictable host-guest strategy exerts the huge potential to improve the fluorescence emission of probes in biosensing [56–59].

Salicylic acid (SA) is a key central signaling molecule in the microenvironment of living plants [60,61]. It can regulate the growth and development processes of plants, with its fluctuation levels directly influencing the survival of plants under various stress conditions [62–66]. Therefore, monitoring the dynamic distribution of SA content is of great significance for crop protection [67–69]. In recent years, several fluorescent probes for SA detection have been developed, typically achieving detection limits in the range of 1–3 μmol/L. However, their applicability remains limited, as they have only been demonstrated in specific biological systems, such as cucumber seedlings or NRK-52E cells [70–75]. Moreover, conventional chemosensors can easily trigger aggregation effects *via* π–π stacking, thereby seriously quenching the fluorescence efficacy and reducing signal sensitivity. To tackle this challenge and upgrading the current fluorescent probes, an intelligent host-guest recognition engineering was used to produce supramolecular fluorescent probes. Initially, an adamantane-groomed rhodamine dye owning a recognized dihydrazide scaffold for SA was synthesized. Subsequently, based on the principle of host-guest recognition, encapsulating certain fragments of RAO within the hydrophobic cavity of CB[8] resulted in a new supramolecular probe, named RAO@2CB[8] (Scheme 1). Interestingly, the topological morphology of the nanoparticles shifted from aggregated hemispheres (RAO) to spheres (RAO@2CB[8]), suggesting that the macrocyclic host could manipulate the molecular aggregation behavior. Following the addition of SA to RAO@2CB[8] led to the morphological transformation into dispersed octahedral supramolecular organic frameworks (SOFs) with strong red fluorescence. Practicably, RAO@2CB[8] exhibited better sensitivity in detecting SA, with a 1.69-fold increase compared to RAO alone. Such substantial improvement indicates that RAO@2CB[8] mitigates the ACQ effect induced by π-π stacking. Finally, fluorescence imaging showed that RAO@2CB[8] could sensitively recognize SA in living HEK-293 cells, cherry radish roots, and salt-stressed pea seedlings.

Given the aforementioned design considerations, a novel adamantane-modified rhodamine bishydrazide dye (RAO) was synthesized through the facile synthetic steps (Scheme S1 in Supporting information). Initially, an adamantane derivative modified with 1,3,4-oxadiazolylhydrazide was obtained *via* cyclization and substitution reactions. Following this, rhodamine B was reacted with $POCl_3$ to produce rhodamine chloride, which was subsequently reacted with the adamantane intermediate *via* a classical condensation reaction, resulting in a rhodamine probe (RAO). Its molecular framework was characterized by NMR and HRMS (Figs. S1–S3 in Supporting information). For successful construction of the supramolecular probe between RAO and CB[8], the possible binding site, stoichiometric ratio and driving forces were investigated by using ^{1}H NMR titration, ultraviolet-visible (UV–vis) spectrum, and HRMS measurement. As delineated in Fig. 1A and Table S1 (Supporting information), with the progressive augmentation of CB[8] to 2.0 equiv., the protons of adamantane (H_{13}–H_{15}) exhibited a gradual upfield shift ($\Delta\delta$ = –0.065, –0.031, –0.057). This observation indicates that the adamantane fragment is specifically sequestered within the cavity of CB[8]. A significant variation on chemical shift of protons H_5–H_6 and H_7–H_{10} ($\Delta\delta$ = 0.301–0.640 ppm) was discovered after adding 1.0 or 2.0 equiv. CB[8], revealing another packaging site between RAO and CB[8]. Given these apparent chemical shifts, we speculate that CB[8] mainly encapsulates two sites: adamantane and xanthene moieties, which provides sufficient steric effects to prevent the stacking of fluorophores [51]. Besides, protons H_1–H_4 and H_{11} gave a downfield movement ($\Delta\delta$ = 0.048–0.136), indicating these protons might locate around the cavity of CB[8] and caused the deshielding effect. Continuous titration of CB[8] into RAO resulted in the chemical shift variations plateauing, signifying an optimal assembly mode of RAO:CB[8] = 1:2. UV–vis spectroscopy further corroborated this assembly behavior (Fig. 1B). UV absorption at 274 nm for RAO progressively reached its nadir when CB[8] was 2 equiv. relative to RAO, substantiating the RAO:CB[8] = 1:2 stoichiometry. HRMS identified the complex as [RAO + 2CB[8] + 5H_2O + H^+] with a molecular weight of 3434.7969, thereby affirming the successful construction of RAO@2CB[8] (Fig. 1C). Scanning electron microscopy (SEM) scrutinized the micro-morphology of RAO and RAO@2CB[8] (Fig. 1D). The topological morphology of RAO transitioned from nanohemispheres to well-defined nanospheres (RAO@2CB[8]), underscoring that host-guest recognition interactions proficiently modulated the aggregation behavior of RAO. Statistical analysis showed that the average particle diameter of RAO and RAO@2CB[8] was 276 and 429 nm, respectively (Fig. 1E), suggesting that the original RAO aggregates were disrupted by host-guest recognition and subsequently reassembled into the new architecture. Additionally, dynamic light scattering (DLS) measurements were performed on RAO, RAO@2CB[8], and RAO@2CB[8] + SA in a MeCN:H_2O (5:5, v/v) solution. As illustrated in Fig. S4 (Supporting information), the particle size distributions were found to be 198–361 nm for RAO and 267–661 nm for RAO@2CB[8], consistent with the statistical sizes observed *via* SEM.

Meanwhile, we have supplemented theoretical calculations related to the RAO@2CB[8] ternary host–guest complex. As shown in Fig. S5 (Supporting information), molecular docking and molecular dynamics simulations revealed that two CB[8] macrocycles simultaneously encapsulated the adamantyl and xanthene moieties at



Scheme 1. Schematic illustrates a predictable supramolecular strategy to effectively solve ACQ problems by regulating molecular aggregation behavior and the fabrication of a model host-guest supramolecular probe RAO@2CB[8] for the sensitive detection of SA.

both ends of the RAO molecule, forming a stable ternary "clamped" host–guest architecture. This unique configuration provided substantial steric hindrance at the molecular level, effectively preventing other RAO molecules from approaching and stacking, while also significantly restricting the conformational flexibility of RAO. Concurrently, multiple noncovalent interactions, particularly hydrogen bonds, were established between RAO and CB[8], further stabilizing the supramolecular network. The following FTIR spectroscopy analyses on RAO, CB[8], and RAO@2CB[8] concurrently confirmed the formation of RAO@2CB[8] supramolecular probe (comprehensive explanations are provided in Fig. S6 in Supporting information). Apart from that, the stability of RAO@2CB[8] was validated under various environmental conditions (Figs. S7 and S8 in Supporting information).

A possible mechanism for regulating molecular aggregation behavior emerges (Scheme 1): Two CB[8] molecules envelop the xanthene and adamantane moieties of RAO, crafting new spherical ternary building blocks RAO@2CB[8], which exhibit profound spatial effects and thwart π-π stacking among the xanthene molecules. These RAO@2CB[8] units subsequently coalesce through potential hydrogen bonding interactions, culminating in the formation of nanosphere structures. Within this spherical architecture, the π-π stacking effect that typically besets the xanthene moiety is curtailed, thereby mitigating the previously troublesome ACQ effect. Subsequent experiments validated this prediction by demonstrating enhanced selectivity and sensitivity in SA detection with supramolecular probes.

The successful fabrication of supramolecular probe RAO@2CB[8] emboldens our pursuit to further authenticate its recognition capability for SA. Upon the introduction of SA, a remarkable enhancement in fluorescence emission intensity at 581 nm was observed, escalating from a baseline of 2.871×10^3 a.u. (RAO@2CB[8]) to an impressive value of 3.137×10^5 a.u. (RAO@2CB[8] + SA), marking an approximate 109-fold amplification (Fig. 2A). This response was superior to RAO+SA (1.856×10^5 a.u.), with a concomitant increase in fluorescence quantum yield (Φ) from 0.21 (RAO + SA) to 0.32 (RAO@2CB[8] + SA). This compelling result indicates that the incorporation of CB[8] adeptly orchestrates the molecular aggregation behavior, thereby augmenting the probe's sensitivity to SA. Additionally, we conducted comparative studies of SA detection capabilities between the two probes (RAO and RAO@2CB[8]) in organic solvents (Fig. S9A in Supporting information) and across varying acetonitrile/water ratios (Figs. S9B–F in Supporting information). These results further substantiate that our designed supramolecular probe mitigates the ACQ effect, thereby markedly enhancing detection performance. However, an increment of CB[8] concentration to 3.0 equiv. did not yield a notable change in fluorescence intensity, corroborating that the stoichiometric ratio of CB[8] to RAO remains at 2:1 during the fine-tuned regulation process (Fig. 2B).

Next, we assessed the selectivity of RAO@2CB[8] for SA. When SA analogues, such as acetylsalicylic acid, 4-SA, and 2-aminobenzoic acid, were introduced, only marginal changes in fluorescence intensity were observed (these analogues are depicted in Fig. S10 in Supporting information). However, the fluorescence

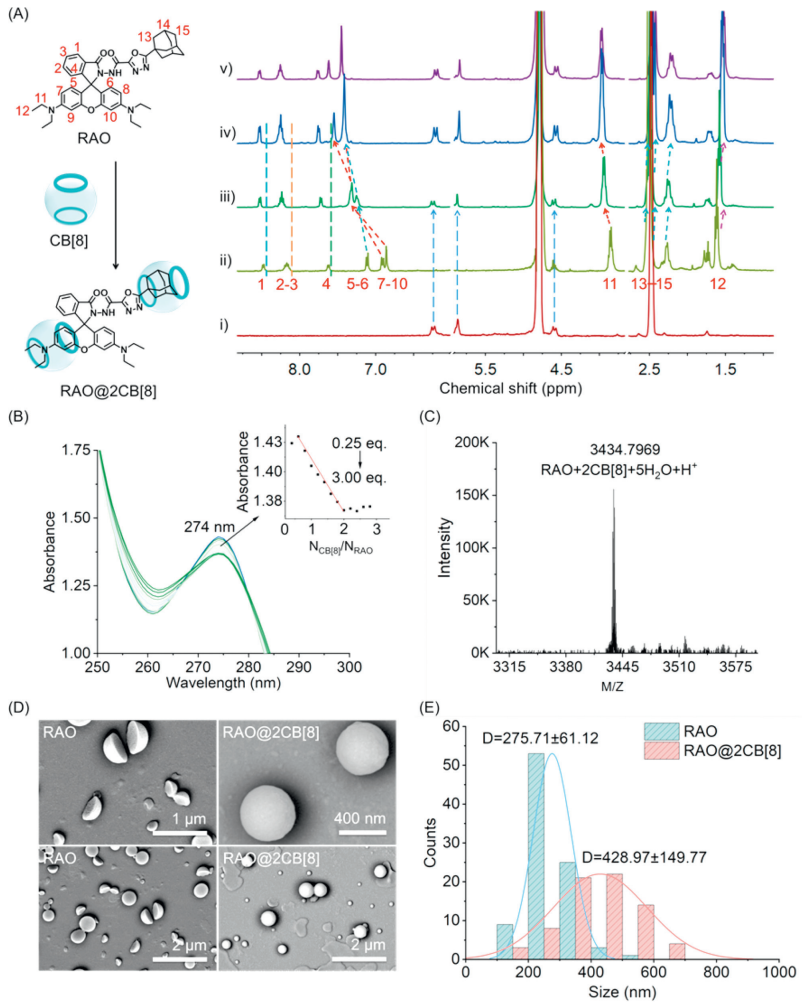


Fig. 1. (A) Partial ^{1}H NMR spectra recorded (400 MHz, 298 K, $CD_3CN:D_2O = 5:5$, v/v) for: (i) CB[8], (ii) RAO (2 mmol/L) in the presence of (iii) 1.0, (iv) 2.0, (v) 3.0 equiv. of CB[8]. (B) UV–vis absorption spectra of RAO (40 μmol/L) with increasing amounts of CB[8] in aqueous solution ($MeCN:H_2O = 5:5$, v/v), inset: UV–vis absorption value change at 274 nm of RAO (40 μmol/L) with different amounts of CB[8]. (C) HRMS spectra of RAO@2CB[8] + $5H_2O + H^+$. (D) SEM images of RAO (40 μmol/L) and RAO@2CB[8] (80 μmol/L CB[8]) in the same solution ($MeCN:H_2O = 5:5$, v/v) at 25 °C. (E) The statistical particle size distribution of RAO and RAO@2CB[8] from above SEM images.

intensity surged significantly upon the addition of SA, underscoring RAO@2CB[8]'s capacity for specific SA recognition (Fig. 2C). UV–vis spectroscopic analysis provided further evidence, revealing that solely SA generated a pronounced absorption band at 560 nm, confirming the probe's selective recognition of SA and the resultant spirolactam ring-opening process (Fig. 2D). Given the potential presence of competitive substances, we proceeded to evaluate the anti-interference performance of RAO@2CB[8]. As illustrated in Fig. 2E, SA analogues failed to trigger the ring-opening reaction of RAO@2CB[8], giving weak fluorescence emissions. In contrast, the fluorescence intensity was markedly enhanced with introducting an equal amount of SA, suggesting the superior anti-interference capability of RAO@2CB[8]. Furthermore, the fluorescence intensity of RAO@2CB[8] exhibited a progressive increase with rising SA concentrations (0–300 μmol/L) (Fig. 2F), displaying a linear correlation within 10–80 μmol/L (Fig. 2G) and 0.27–6.23 μmol/L (Fig. S11 in Supporting information). The limit of detection for SA was determined as 66.7 nmol/L. Job's plots revealed that RAO@2CB[8] and SA interacted in a stoichiometric ratio of 1:1 (Fig. 2H). Additionally, the binding constant was $K_a = 6.91 \times 10^4$ L/mol (Fig. 2I), affirming the robust interaction between RAO@2CB[8] and SA. Lastly, the topological change of RAO@2CB[8] triggered by SA was substantiated using SEM. Clearly, RAO@2CB[8]-assembled nanospheres underwent a striking transformation into well-dispersed octahedral SOFs (Fig. 2J), suggesting that a perceptible interaction occurs between SA and the probe, and leads to reassemble these building blocks.

The enhancive efficacy of RAO@2CB[8] on sensitive detection of SA were postulated. Initially, SA with two hydroxyl groups engages in robust hydrogen bonding interactions with the spirolactam-hydrazide moiety of RAO@2CB[8], instigating a ring-opening reaction. Within this new product, two CB[8] encapsulate the xanthene and adamantane units, showcasing pronounced spatial effects that effectively hinder internal rotation and vibrational relaxation processes, resulting in a enhancive fluorescence emission. Next, the reorganized SOF-based unit (RAO@2CB[8] + SA) began to assemble and eventually formed octahedral assemblies, a kind of three-dimensional architectures with steric and structural stability (Scheme 1). Such meticulous encapsulation *via* the smart supramolecular technology adeptly mitigates the ACQ effect.

The transformation process and luminescent property of these octahedral SOFs were investigated using SEM and confocal laser scanning microscopy (CLSM) imaging. Figs. 3Aa–c depicted how incremental additions of SA to 0.5–2.5 equiv. caused the changes from nanospheres (RAO@2CB[8]). Notably, higher concentrations of SA resulted in more pronounced geometric feature, indicating that the amount of SA is crucial for producing the newly ring-opened SOF-based building block. Intriguingly, increasing the SA concen-

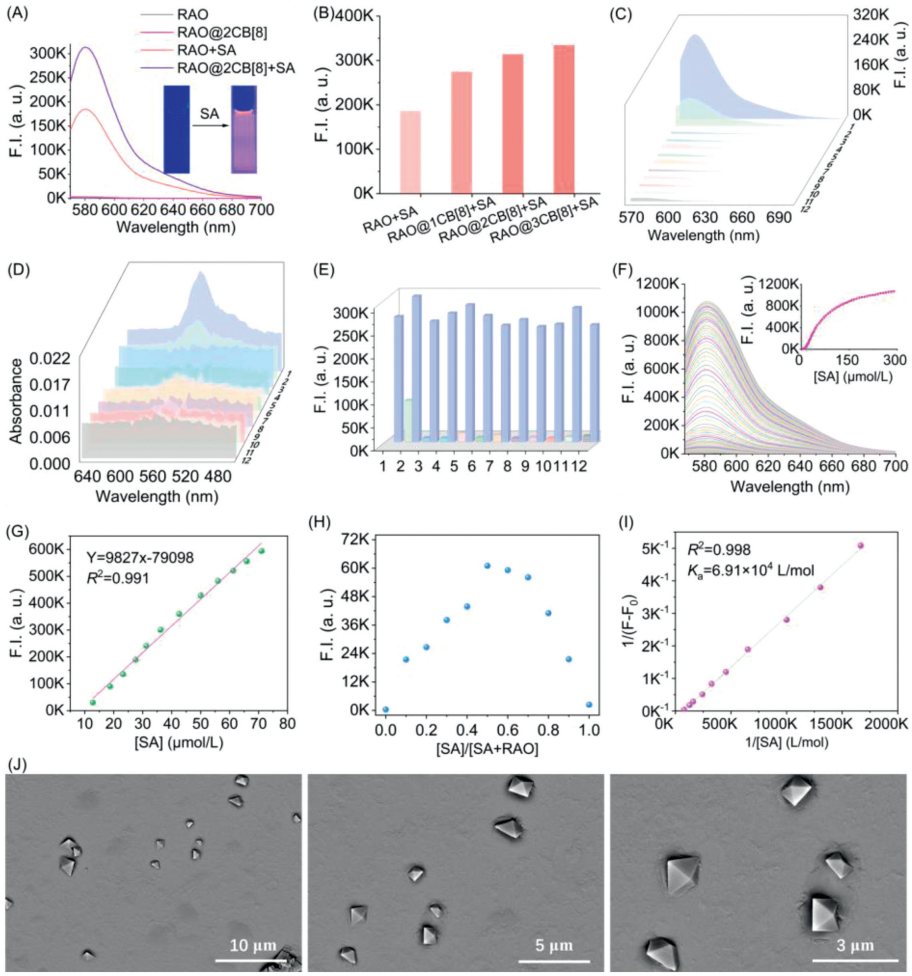


Fig. 2. (A) Fluorescence spectra of RAO (10 μmol/L), RAO@2CB[8] (10 μmol/L), RAO + SA (10 μmol/L + 50 μmol/L), RAO@2CB[8] + SA (10 μmol/L + 50 μmol/L) in MeCN–H_2O solution, MeCN:H_2O = 5:5, v/v, λ_{ex} = 561 nm, slits: 3.0/3.0 nm. (B) The fluorescence intensity at 581 nm of RAO with 1.0–3.0 equiv. CB[8] upon the addition of 50 μmol/L SA. (C) Fluorescence spectra of RAO@2CB[8] (10 μmol/L) upon the addition of SA and its analogues (50 μmol/L) in the mixed solution (MeCN:H_2O = 5:5, v/v), (1) blank, (2) ASA, (3) CaT, (4) MeSA, (5) 2-MeBA, (6) 2-NH_2BA, (7) phenol, (8) 2-MeOBA, (9) 3-OHBA, (10) SAH, (11) 4-OHBA, (12) BA. (D) UV–vis absorption spectra of RAO@2CB[8] (10 μmol/L) upon addition of SA and its analogues (50 μmol/L) in the mixed solution (MeCN:H_2O = 5:5, v/v). (E) Competition experiments for adding 50 μmol/L SA into the premixed solution consisting of RAO@2CB[8] (10 μmol/L) with various SA analogues (50 μmol/L), experimental conditions: λ_{ex} = 561 nm, slits: 3.0/3.0 nm, MeCN:H_2O = 5:5, v/v. (F) Fluorescence titration spectra of RAO@2CB[8] (10 μmol/L) induced by SA (0–300 μmol/L) in the mixed solution, inset: changes of the emission intensity at 581 nm. (G) The linear fluorescence change of RAO@2CB[8] (10 μmol/L) with SA (10–80 μmol/L) at 581 nm. (H) Job's plots of RAO@2CB[8] with SA, λ_{ex} = 561 nm, slits: 3.0/3.0 nm. (I) Benesi-Hildebrand plots of RAO@2CB[8] with SA, the binding constant ($K_a = 6.91 \times 10^4$ L/mol) was determined by fluorescence method, experiment conditions: MeCN:H_2O = 5:5, λ_{ex} = 561 nm, slits: 3.0/3.0 nm. (J) SEM images of RAO@2CB[8] (40 μmol/L) + 5 equiv. SA in the same solution (MeCN:H_2O = 5:5, v/v) at 25 °C.

tration to 5.0 equiv. led to a complete transformation, previously showing only partial edges, into sharply defined octahedrons (Fig. 3Ad). Furthermore, a noteworthy increase in the particle size of the newly formed octahedra was observed, reaching its maximum at 5.0 equiv. of SA (Fig. 3B). This observation aligned with the DLS measurements for RAO@2CB[8] + 5SA, which showed particle sizes ranging from 1209 nm to 3477 nm (Fig. S4C in Supporting information). Remarkably, in the absence of CB[8], RAO + 5SA exhibited a highly aggregated microstructure with a blurred appearance (Fig. 3Ae). These findings underscore a crucial insight: aromatic fluorophores containing xanthene with π-conjugated systems are highly prone to π-π stacking, leading to the ACQ effect. However, CB[8] encapsulates the conjugated fluorophores to provide spatial effects, mitigating ACQ and enhancing fluorescence emission. Additionally, the dropwise addition of SA analogues (3-OHBA, 4-OHBA or BA) to RAO@2CB[8] failed to form octahedrons (Fig. S12 in Supporting information). This outcome is attributed to the inability of these acids to ring-open the probe. CLSM imaging results provided compelling evidences (Figs. 3Ca–e). The fluorescence emission of the RAO@2CB[8] + SA system gradually intensified with increasing SA concentrations (1.0–5.0 equiv.). In contrast, the RAO + 5SA system, devoid of CB[8], exhibited densely packed small particles and weak fluorescence (Fig. 3Cf). The following statistical analysis of the fluorescence images was illustrated in Fig. S13 (Supporting information). Clearly, upon the addition of 5.0 equiv. of SA, the fluorescence signal of RAO@2CB[8] + 5SA was notably higher than RAO + 5SA, demonstrating the supramolecular probe's dual capability in alleviating ACQ and boosting sensitivity. However, SA analogues did not exhibit these changes in fluorescence (Fig. S14 in Supporting information). These results highlight the pivotal role of CB[8]'s rigid cavity in constraining the intramolecular movements of RAO and suppressing π-π stacking behaviors. To confirm whether CB[8] continues to encapsulate the ring-opened rhodamine product of RAO, ^{1}H NMR spectroscopy was performed on RAO@2CB[8] with 5.0 equiv. of SA (Fig. 3D). After adding SA to RAO@2CB[8], the adamantly protons (H_{13-15}) did not gave any changes in chemical shift, revealing the formation of CB[8]-adamantane inclusion at this location. For the xanthene part, the protons H_{5-6} and H_{7-10} of xanthene shifted downfield slightly, which was attributed to the occurrence of the ring-

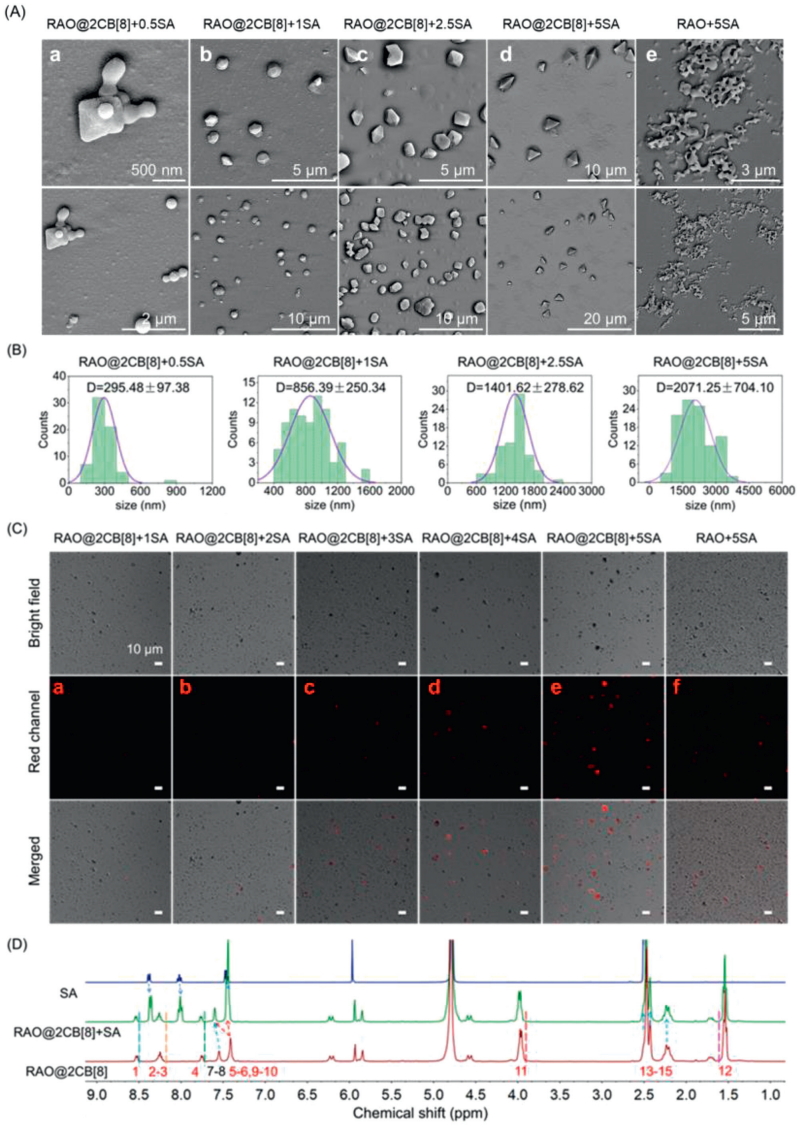


Fig. 3. (A) SEM images of SA titration: (a) RAO@2CB[8] (40 μmol/L) + 0.5 equiv. SA (20 μmol/L), (b) RAO@2CB[8] + 1.0 equiv. SA, (c) RAO@2CB[8] + 2.5 equiv. SA, (d) RAO@2CB[8] + 5.0 equiv. SA, (e) RAO + 5 equiv. SA. (B) Particle size distributions for RAO@2CB[8] + 0.5 (1.0, 2.5, or 5.0) equiv. SA. (C) CLSM imaging for RAO@2CB[8] (40 μmol/L) + (a) 1.0 equiv. SA (40 μmol/L), (b) 2.0 equiv. SA, (c) 3.0 equiv. SA, (d) 4.0 equiv. SA, or (e) 5.0 equiv. SA, (f) RAO (40 μmol/L) + 5 equiv. SA. (D) Partial ^{1}H NMR spectra recorded (400 MHz, 298 K, $CD_3CN:D_2O = 5:5$, v/v) for RAO (2 mmol/L), molar ratio RAO:CB[8]:SA = 1:2:5, and SA (10 mmol/L).

opening reaction at the spirolactam site (Table S2 in Supporting information). Given the minor fluctuations in chemical shift and the preference of CB[8] for cations, we preliminary inferred that CB[8] was also attached to the xanthene moiety. Simultaneously, the protons belonging to SA shifted upfield (Table S3 in Supporting information), likely due to the shielding effect after forming hydrogen bonding with RAO@2CB[8]. In summary, compared to RAO alone, RAO@2CB[8] demonstrates significantly heightened sensitivity to SA.

The remarkable sensitivity of probe RAO@2CB[8] in precisely recognizing SA inspired us to delve deeper into the fluorescence imaging capability. Thus, the roots of cherry radish were randomly used to detect SA in the living microenvironment. Firstly, the roots were incubated with RAO@2CB[8] or RAO for 15 min, followed by an additional 15-min incubation with SA to perform fluorescent imaging. As depicted in Fig. S15a (Supporting information), the red channels of both RAO@2CB[8] and RAO groups exhibited no fluorescence in the absence of SA. However, upon treatment with exogenous SA, both the RAO@2CB[8] and RAO groups displayed pronounced red fluorescence. Quantitative analysis revealed that RAO@2CB[8] + SA group demonstrated a superior fluorescence strength of approximately three times higher than the RAO + SA group (Fig. S15b in Supporting information). This significant enhancement underscores the successful employment of CB[8]-mediated supramolecular probes for enhancing the sensitive detection of bioactive species in living environments, confirming our initial design goal of using smart supramolecular strategies to overcome the ACQ challenge.

SA plays an important role in regulating defense responses against diverse environmental stresses, particularly salinity [60–64]. Therefore, real-time tracking the dynamic distribution of SA in salt-stressed environments can advance our understanding of SA-induced molecular mechanisms underlying this event. Before doing the bioimaging with the supramolecular probe RAO@2CB[8], we firstly investigated SA-mediated plant growth under salt-stress conditions. As displayed in Fig. 4A and Fig. S16 (Supporting information), co-cultivation with SA (25 μmol/L) under salt-stressed conditions improves seed germination and growth of white pea seedlings. Given the above surveys, the effectiveness of probe RAO@CB[8] for detecting SA was corroborated by laser confocal

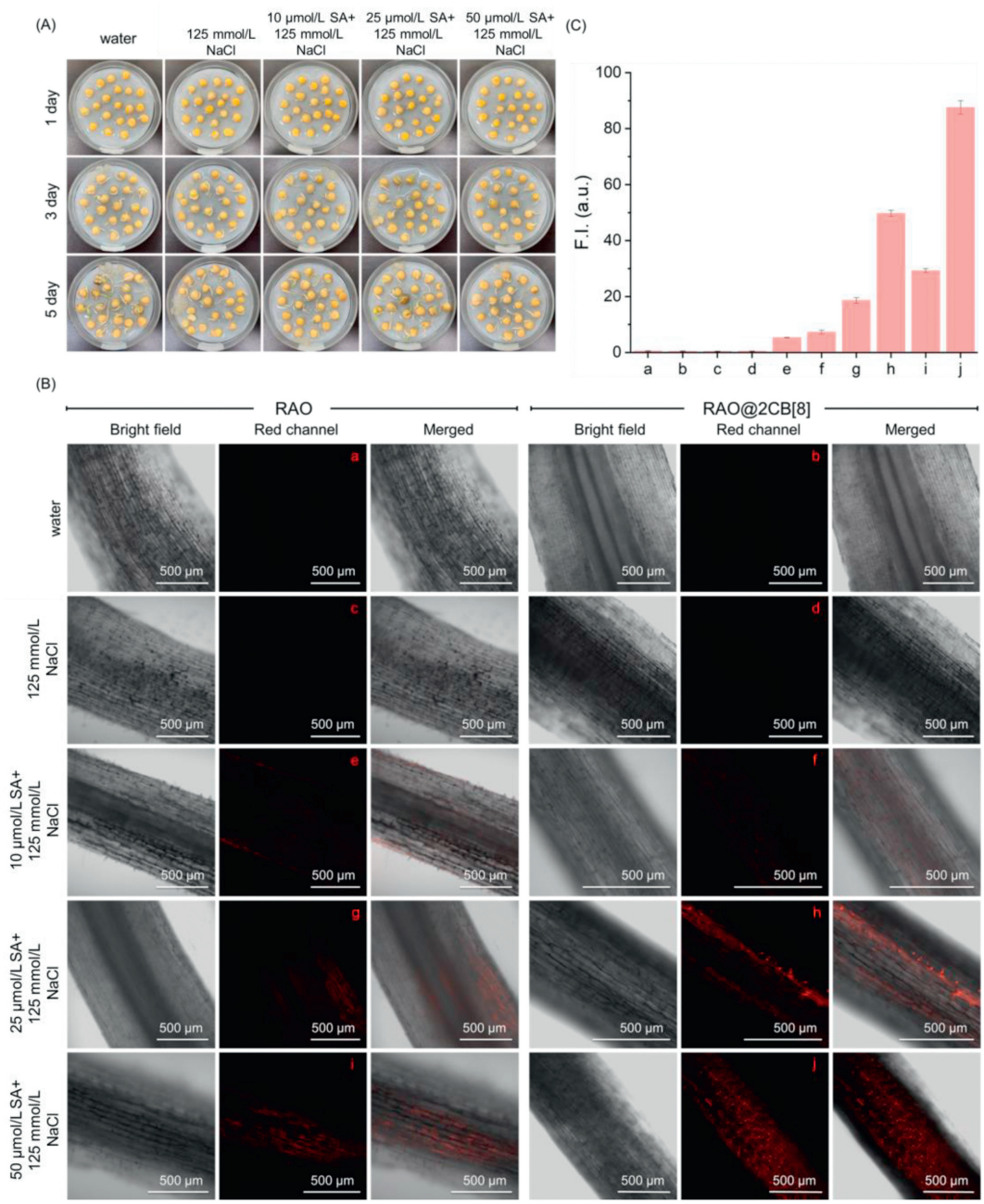


Fig. 4. (A) Seed germination experiments of white peas under salt-stressed conditions (125 mmol/L NaCl) with different concentrations of SA (10, 25, and 50 μmol/L). (B) Confocal microscope images of salt-stressed white pea seedling roots after being incubated with 30 μmol/L RAO or RAO@2CB[8] (60 μmol/L CB[8]) for 15 min at 25 °C, $\lambda_{ex} = 567$ nm; $\lambda_{em} = 593$ nm. (C) The average fluorescence intensity of red channels in white pea roots excited by confocal microscopy.

testing. As shown in Figs. 4B and C, RAO@2CB[8] groups displayed striking red fluorescence for recognizing SA in a dose-dependent manner (Figs. 4B(f, h, j) and C(f, h, j)). At 25 μmol/L (SA), the average fluorescence intensity of RAO@2CB[8] + SA group was approximately 2.7 times higher than that of the RAO + SA group. When SA was elevated to 50 μmol/L, the fluorescence of RAO@2CB[8] + SA group was about 3 times greater than the RAO + SA group. These encouraging outcomes disclosed that a highly efficient supramolecular probe RAO@2CB[8] was developed, demonstrating superior performance for bioimaging applications in intricate environments. In addition, both RAO@2CB[8] and RAO did not exhibit any potential phytotoxicity to white pea seedlings (Figs. S17 and 18 in Supporting information).

SA serves critical roles in both medical therapy and diagnostics. As a topical agent (0.2 %–1.5 %), it effectively treats psoriasis, calluses, and keratosis pilaris [76,77]. However, SA imbalance can cause neurotoxicity, organ dysfunction, and developmental toxicity [78,79]. This underscores the need for reliable SA monitoring methods in pharmaceutical and biological systems. In this section, HEK-293 cells were employed to demonstrate the imaging potential of probe RAO@2CB[8]. As presented in Fig. S19a (Supporting information), probes RAO@2CB[8] and RAO could induce the generation of red fluorescence in SA-treated cell components. In particular, the average fluorescence intensity of RAO@2CB[8] + SA group was approximately 4.5 times higher than that of RAO + SA group (Fig. S19b in Supporting information).

In conclusion, a predictable host-guest recognition engineering, which could regulate molecular aggregation behaviors from "π–π stacking" to a "relaxing" state at the molecular level, was used to fabricate a rhodamine-based supramolecular fluorescent

probe, named RAO@2CB[8]. This ternary conjugate exhibited superior profiles for selectively detecting a key plant signaling ingredient, SA. The related fluorescence quantum yield was enhanced from 0.21 (RAO+SA) to 0.32 (RAO@2CB[8] + SA), with a lower LOD of 66.7 nmol/L (Table S4 in Supporting information). During these processes, the topological morphology transformed from hemisphere (RAO) to spheroid (RAO@2CB[8]), and final fluorescent octahedral SOFs (RAO@2CB[8] + 5 equiv. SA). In complicated living biological systems, RAO@2CB[8] displayed good cell-permeability and could realize the highly precise imaging of SA in HEK-293 cells, radish roots, and salt-stressed pea seedlings. This facile supramolecular strategy built in this study provides guidance for alleviating ACQ effect *via* fundamentally fine-tuning molecular aggregation behaviors. We anticipate the development of more sensitive supramolecular probes for precise analyte detection across multiple disciplines.

Declaration of competing interest

The authors declare that they have no known competing financial interests or personal relationships that could have appeared to influence the work reported in this paper.

CRediT authorship contribution statement

Juan Liu: Writing – review & editing, Visualization, Validation, Software, Methodology, Investigation, Formal analysis, Data curation. **Tian Wang:** Visualization, Formal analysis, Data curation. **Jinghan Yang:** Writing – review & editing, Visualization. **Peiyi Wang:** Writing – review & editing, Writing – original draft, Investigation, Funding acquisition, Conceptualization.

Acknowledgments

We acknowledge funds from Innovation Program for High-level Talents of Guizhou Province (No. GCC[2023]008), Guizhou Provincial S&T Project (No. ZK[2022]017), Research and Innovation Team of Guizhou University (No. Guidakechuangtuan[2023]03), Natural Science Special Project of Guizhou University (No. Guidazhuanjihe[2024]02).

Supplementary materials

Supplementary material associated with this article can be found, in the online version, at doi:10.1016/j.cclet.2025.111782.

References

[1] L. Wu, A.C. Sedgwick, X. Sun, et al., Acc. Chem. Res. 52 (2019) 2582–2587.
[2] D. Zhang, H. Liu, T. He, et al., Small 17 (2021) 2005113.
[3] M.K. Goshisht, N. Tripathi, G.K. Patra, et al., Chem. Sci. 14 (2023) 5842–5871.
[4] R. Sivakumar, N.Y. Lee, et al., Coord. Chem. Rev. 501 (2024) 215563.
[5] J. Zhao, J. Chen, S. Ma, et al., Acta Pharm. Sin. B 8 (2018) 320–338.
[6] N.C. Payne, A.S. Kalyakina, K. Singh, et al., Nat. Chem. Biol. 17 (2021) 1168–1177.
[7] Y. Zhu, B. Wu, X. Gao, et al., Biosens. Bioelectron. 244 (2024) 115809.
[8] Y. Kang, N. Fei, L. Niu, et al., Chin. Chem. Lett. 30 (2019) 1791–1798.
[9] A.S. Burange, K.G. Gadam, P.S. Tugaonkar, et al., Environ. Chem. Lett. 19 (2021) 3283–3314.
[10] Y. Zhu, L. Lin, H. Lai, et al., Adv. Sci. 11 (2023) 2307659.
[11] Z. Zhu, D. Zhang, J. Chen, et al., Mater. Horiz. 10 (2023) 4868–4881.
[12] X. Kang, L. Zhang, L. Yang, et al., Chem. Eng. J. 476 (2023) 146923.
[13] C. Zeng, Y. Tan, L. Sun, et al., ACS Appl. Mater. Interfaces 15 (2023) 17664–17674.
[14] Y. Zhang, Y. Zhao, Z. Han, et al., Angew. Chem. Int. Ed. 59 (2020) 23261–23267.
[15] H. Lu, Y. Wang, S.K. Hill, et al., Angew. Chem. Int. Ed. 62 (2023) e202311224.
[16] W. Li, J. Wang, Y. Xie, et al., Prog. Org. Coat. 120 (2018) 1–9.
[17] J. Qi, X. Hu, X. Dong, et al., Adv. Drug Deliv. Rev. 143 (2019) 206–225.
[18] J. Wang, H. Liu, M. Wu, et al., Talanta 205 (2019) 120095.
[19] Y. Jin, R. Sun, G. Li, et al., Spectrochim. Acta A: Mol. Biomol. Spectrosc. 294 (2023) 122558.
[20] Y. Tang, H. Huang, B. Peng, et al., J. Mater. Chem. A 8 (2020) 16542–16550.
[21] R. Guo, S. Ye, Y. Wang, et al., J. Mater. Chem. C 9 (2021) 13392–13401.
[22] L. Ren, Y.J. Kim, S.Y. Park, et al., J. Mater. Chem. B 4 (2016) 4832–4838.
[23] F. Zhang, X. Zheng, E. Liu, et al., J. Ind. Eng. Chem. 46 (2017) 397–403.
[24] X. Zhang, S. Shen, D. Liu, et al., Chem. Sci. 14 (2023) 2928–2934.
[25] M. Park, Y. Jeong, H.S. Kim, et al., Adv. Funct. Mater. 31 (2021) 2102741.
[26] N. Zhang, D. Zhang, J. Zhao, et al., Dalton Trans. 48 (2019) 6794–6799.
[27] X. Yuan, Z. Wang, L. Li, et al., Mater. Chem. Front. 3 (2019) 1097–1104.
[28] G. Lutzweiler, A.N. Halili, N.E. Vrana, et al., Mater. Chem. Front. 12 (2020) 602.
[29] F.J. Maksoud, M.F. Velázquez de la Paz, A.J. Hann, et al., J. Mater. Chem. B 10 (2022) 8111–8165.
[30] A. Reisch, A.S. Klymchenko, et al., Small 12 (2016) 1968–1992.
[31] H.S. Jung, K.J. Cho, Y. Seol, et al., Adv. Funct. Mater. 28 (2018) 1801252.
[32] G. Della Pelle, A.D. López, M.S. Fiol, et al., Int. J. Mol. Sci. 22 (2021) 6914.
[33] C. Jeong, S. Uthaman, B. Bagheri, et al., J. Control. Release 329 (2021) 50–62.
[34] J. Xin, S. Han, M. Zheng, et al., Chin. Chem. Lett. 35 (2024) 109165.
[35] T. Matsuno, S. Sato, A. Yokoyama, et al., Angew. Chem. Int. Ed. 55 (2016) 15339–15343.
[36] W.T. Gallonde, C. Poidevin, F. Houard, et al., Angew. Chem. Int. Ed. 62 (2023) e202313696.
[37] H. Ju, Z. Yin, Z. Demchuk, et al., Adv. Funct. Mater. 34 (2024) 2402165.
[38] N. Zhang, W.Y. Lo, Z. Cai, et al., Nano Lett. 17 (2017) 308–312.
[39] R.M. Veedu, N. Niemeyer, N. Bäumer, et al., Angew. Chem. Int. Ed. 62 (2023) e202314211.
[40] A.C. Bhasikuttan, H. Pal, J. Mohanty, et al., Chem. Commun. 47 (2011) 9959–9971.
[41] S.R. Shariati Pour, S. Oddis, M. Barbalinardo, et al., Molecules 28 (2023) 2528.
[42] K. Jalani, A.D. Das, R. Sasmal, et al., Nat. Commun. 11 (2020) 3967.
[43] A. Sarkar, R. Sasmal, A. Das, et al., Chem. Commun. 57 (2021) 3937–3940.
[44] M. Ponce-Vargas, C. Lefebvre, J.C. Boisson, E. Hénon, J. Chem. Inf. Model. 60 (2020) 268–278.
[45] C. Stoffelen, J. Huskens, Small 12 (2016) 96–119.
[46] Y. Chen, S. Sun, D. Lu, et al., Chin. Chem. Lett. 30 (2019) 37–43.
[47] W. Liu, W. Xu, H.H. Luan, et al., Biosens. Bioelectron. 241 (2023) 115678.
[48] B.V.K.J. Schmidt, K. Barner, C. Christopher, et al., Angew. Chem. Int. Ed. 56 (2017) 8350–8369.
[49] X. Zhou, X. Su, P. Pathak, et al., J. Am. Chem. Soc. 139 (2017) 13916–13921.
[50] Y. Zhao, M. Wei, L. Tan, et al., Small 20 (2024) 2308164.
[51] X.L. Ni, S. Chen, Y. Yang, et al., J. Am. Chem. Soc. 138 (2016) 6177–6183.
[52] J. Barrio, J. Liu, R.A. Brady, et al., J. Am. Chem. Soc. 141 (2019) 14021–14025.
[53] D. Wu, J. Wang, X. Du, et al., J. Nanobiotechnol. 22 (2024) 235.
[54] C. Wang, Y. Liu, Y. Liu, et al., Small 18 (2022) 2201821.
[55] L. Yang, Y. Li, H. Zhang, et al., Chin. Chem. Lett. 34 (2023) 108108.
[56] H. Ma, W. Xu, X. Tang, et al., CCS Chem. 7 (2025) 832–842.
[57] D. Wu, Y. Wang, N. Wu, et al., J. Hazard. Mater. 479 (2024) 135751.
[58] J. Zhou, S. Hou, J. Zhang, et al., Chin. Chem. Lett. 32 (2021) 725–728.
[59] B. Hua, L. Shao, Z. Zhang, et al., Sens. Actuators B: Chem. 255 (2018) 1430–1435.
[60] P. Ding, Y. Ding, et al., Trends Plant Sci. 25 (2020) 549–565.
[61] Y. Peng, J. Yang, X. Li, et al., Annu. Rev. Plant Biol. 72 (2021) 761–791.
[62] M. Iqbal, M. Ashraf, et al., J. Integr. Plant Biol. 49 (2007) 1003–1015.
[63] V. Kovács, O.K. Gondor, G. Szalai, et al., J. Hazard. Mater. 280 (2014) 12–19.
[64] A.B. Wani, H. Chadar, A.H. Wani, et al., Environ. Chem. Lett. 15 (2017) 101–123.
[65] C. Kaya, M. Ashraf, M.N. Alyemeni, et al., J. Hazard. Mater. 399 (2020) 123020.
[66] X. Jia, L. Wang, H. Zhao, et al., Mol. Plant 16 (2023) 245–259.
[67] M. Sivakumar, M. Sakthivel, S.M. Chen, et al., J. Colloid Interface Sci. 501 (2017) 350–356.
[68] X.B. Zhang, B.H. Feng, H.M. Wang, et al., J. Integr. Plant Biol. 60 (2018) 160–172.
[69] Y. Shi, W. Li, X. Hu, et al., Food Chem. 434 (2024) 137260.
[70] Z.M. Fang, L.L. Zhang, J.J. Wang, et al., Arabian J. Chem. 16 (2023) 104476.
[71] A. Kumar, A. Pandith, H.S. Kim, J. Luminesc. 172 (2016) 309–316.
[72] M.W. Ahmad, B.Y. Kim, H.S. Kim, New J. Chem. 38 (2014) 1711–1716.
[73] A. Kumar, M.K. Ghosh, C.H. Choi, et al., RSC Adv. 5 (2015) 23613–23621.
[74] A. Pandith, G. Hazra, H.S. Kim, Spectrochim. Acta A: Mol. Biomol. Spectrosc. 178 (2017) 151–159.
[75] C. Chen, L.L. Yang, A.L. Tang, et al., J. Agric. Food Chem. 68 (2020) 4844–4850.
[76] Z.M. Fang, L.L. Zhang, J.J. Wang, et al., Arab. J. Chem. 16 (2023) 104476.
[77] G.K. Hogendoorn, S.C. Bruggink, M.N.C. de Koning, et al., Br. J. Dermatol. 178 (2018) 253–260.
[78] D.P. Davis, G.P. Daston, M.R. Odio, et al., Toxicol. Lett. 84 (1996) 135–141.
[79] R. Freitas, S. Silvestro, F. Coppola, et al., Aquat. Toxicol. 214 (2019) 105258.